Journal of Nuclear Materials 397 (2010) 80–91

Contents lists available at ScienceDirect

Journal of Nuclear Materials

journal homepage: www.elsevier.com/locate/jnucmat

Mechanical behaviors of the dispersion nuclear fuel plates induced by fuel particle swelling and thermal effect II: Effects of variations of the fuel particle diameters

Shurong Ding *, Qiming Wang, Yongzhong Huo

Department of Mechanics and Engineering Science, Fudan University, Shanghai 200433, China

ARTICLE INFO

Article history:
Received 27 September 2009
Accepted 18 December 2009

ABSTRACT

In order to predict the irradiation mechanical behaviors of plate-type dispersion nuclear fuel elements, the total burnup is divided into two stages: the initial stage and the increasing stage. At the initial stage, the thermal effects induced by the high temperature differences between the operation temperatures and the room temperature are mainly considered; and at the increasing stage, the intense mechanical interactions between the fuel particles and the matrix due to the irradiation swelling of fuel particles are focused on. The large-deformation thermo–elasto-plasticity finite element analysis is performed to evaluate the effects of particle diameters on the in-pile mechanical behaviors of fuel elements. The research results indicate that: (1) the maximum Mises stresses and equivalent plastic strains at the matrix increase with the fuel particle diameters; the effects of particle diameters on the maximum first principal stresses vary with burnup, and the considered case with the largest particle diameter holds the maximum values all along; (2) at the cladding near the interface between the fuel meat and the cladding, the Mises stresses and the first principal stresses undergo major changes with increasing burnup, and different variations exist for different particle diameter cases; (3) the maximum Mises stresses at the fuel particles rise with the particle diameters.

1. Introduction

With development of nuclear energy all over the world, a large amount of nuclear wastes [1] with heavy radioactivity have been produced and will be produced. Effective methods to dispose of these wastes should be adopted. An alternative is to make use of the dispersion nuclear fuel element as a carrier to consume them in the commercial nuclear reactors [2,3]. Besides, the dispersion nuclear fuel elements have been widely used in the research and test reactors since the Reduced Enrichment for Research and Test Reactors (RERTR) program started in 1970s. With the conversion need of research reactors from high-enriched uranium (HEU) to low-enriched uranium (LEU) with a U^{235} content of less than 20%, the dispersion nuclear fuel elements are widely adopted owing to their high uranium density [4,5], several kinds of dispersion fuels such as the U_3Si_2 dispersion fuel are formally qualified for reactor use and a good many research and test reactors have been converted to LEU fuels. Because of their important applications, the relative researches [6–8] to further improve the performances of the current dispersion fuel elements keep all the while.

In the demanding environment of nuclear reactors, the in-pile thermal–mechanical behaviors of dispersion fuel elements are of complexity. In the fuel meat, the fuel particles attacked continually by the neutrons produce fission heat which results in existence of the inhomogeneous temperature field within the fuel element; and in the meantime the solid and inert gas fission products lead to the irradiation swelling of fuel particles with increasing burnup and the configuration of the fuel element will be updated accordingly; the fission gas would migrate to the free volumes with rise of burnup and would form the bubble nucleus if caught by flaws, dislocation, and cavity on the grain boundary, and the bubbles would grow with absorption of the liberated fission gas [9]. The nuclear experiment [10] indicated that the microstructure of the fuel meat could remarkably influence the in-pile mechanical behaviors of dispersion nuclear fuel elements. Thus, in order to assess the lifetime of a dispersion fuel element and optimize its microstructure, the effects of the microstructure on its in-pile mechanical behaviors should be investigated.

Besides the relative experimental researches [11], the numerical simulations are playing a more and more important role in explaining the experiment results and in the optimal design because they can supply the engineers with a predictive tool and shorten the design period. Recently, the relative researches on the dispersion fuel plate with the finite element method (FEM) appeared and some

* Corresponding author.
E-mail address: dsr1971@163.com (S. Ding).

0022-3115/$ - see front matter © 2010 Elsevier B.V. All rights reserved.
doi:10.1016/j.jnucmat.2009.12.012

specific codes for the thermal and thermal–mechanical analysis were developed and were being upgraded, including FASTDART [12,13], PLATE [14,15], MAIA [16,17] and DART-TM [18] and so on. In these studies, the dispersion fuel meat was generally treated as homogeneous and the modeling was two-dimensional, that is, the mutual actions between the fuel particles and the matrix are not taken into account. Böning and Petry [19] simulated the irradiation swelling of the full-sized U_3Si_2–Al fuel plate whose meat was regarded as a homogeneous one, revealing that the dispersion fuel plate with the particle volume fraction being only about 20% had presented a remarkably swelling ratio under the studied irradiation condition. However, the interactions between the fuel particles and the metal matrix should be considered in order to optimize the fuel meat. Van Duyn [3] studied the PuO_2–Zr rod-like dispersion fuel element with FEM, taking account of the mutual mechanical interactions between the fuel particles and the matrix, while the in-pile mechanical behaviors were simplified. In our previous researches [20,21] the thermal and mechanical behaviors within the plate-type dispersion nuclear fuel element were studied, but the actual cladding structure was not drawn into consideration and the temperature field with increasing burnup was supposed to be the same as the one induced by the thermal effect. In a word, the effects of the micro-structures on the in-pile mechanical behaviors of dispersion nuclear fuel elements are rarely simulated.

In this study, the effects of fuel particle sizes on the in-pile mechanical behaviors of dispersion nuclear fuel elements are investigated through numerical simulations. Different three-dimensional finite element models are developed respectively for different particle diameter cases, which might simulate both the micro stress–strain field and the macro deformation along the thickness. The total burnup is divided into two analysis step. The first analysis step corresponds to the initial burnup stage in which the thermal–mechanical behaviors are mainly induced by the temperature variations; and the second analysis step takes account of the effects of the particle swelling and the updated configuration of the fuel element using the large-deformation thermo–elasto-plasticity finite element method. The obtained research results are expected to be helpful to the optimal design of dispersion fuel elements.

2. Basic formula and relations

One kind of typical dispersion fuel element is investigated in this study, having an alloy cladding and a meat with the fuel particles dispersed in a metal matrix. Owing to easy acquirements of the material parameters of uranium dioxide (UO_2) and zircaloy, they are set as the materials of the fuel particles and the metal matrix (or the cladding).

Since the fission heat and the gradually updated configuration induced by the fuel swelling lead to variations of the temperature field, the in-pile mechanical behaviors of the fuel element might be remarkably affected due to the temperature-dependence of the material parameters. In order to determine the stress–strain field, the temperature field should be calculated first. Thus, the whole burnup can be divided into lots of time steps, and at every time step, the temperature field can be regarded as a steady one. With the temperature field at every time step determined, the relative mechanical field can be calculated subsequently. It can be called a thermal–mechanical coupling analysis problem. In this section, the basic equations and the required material parameters are to be given.

2.1. Heat conduction analysis model

For steady-state thermal problems, the temperature distributions of the fuel elements are influenced by the thermal conductivities of the fuel particles and matrix, the fission rates of the fuel particles and the heat transfer coefficient between the cladding and the coolant water. So, temperature-dependent material properties will be given.

2.1.1. The heat generation rate of the fuel particles

The heat generation rate of the fuel particles is obtained as

$$\dot{q} = c \cdot \dot{f} \tag{1}$$

where $c = 3.204 \times 10^{-11}$ J/fission is the generated heat energy every fissionning event and $\dot{f}$ is the fission rate of the fuel particles.

2.1.2. Thermal conductivities of fuel particles

The model of thermal conductivities of fuel particles improved by Lucuta et al. [22] consists of five contributions and can be expressed as

$$K_{UO_2} = K_0 \cdot FD \cdot FP \cdot FM \cdot FR \tag{2}$$

where K_0 is Harding's expression for the thermal conductivity of unirradiated UO_2; *FD* quantifies the effect of dissolved fission products; *FP* describes the effect of precipitated solid fission products; *FM* is the modified Maxwell factor for the effect of the pore and fission-gas bubbles; *FR* characterizes the effect of radiation damage.

2.1.3. Thermal conductivities of matrix and cladding

For the Zircaloy matrix and cladding, its thermal conductivity from the room temperature to the melting point can be expressed by [23]:

$$k = 7.51 + 2.09 \times 10^{-2}T - 1.45 \times 10^{-5}T^2 + 7.67 \times 10^{-9}T^3 \tag{3}$$

where T denotes the temperature in Kelvin.

2.2. The constitutive model of fuel particles

The thermal expansion of UO_2 fuel particles relative to 300 K can be expressed as [24]

$$\Delta l/l_0 = -3.0289 \times 10^{-4} + 8.4217 \times 10^{-6}(T - 273) + 2.1481 \times 10^{-9}(T - 273)^2 \tag{4}$$

where T denotes the temperature in Kelvin with the application range from 300 K to 1530 K.The elastic modulus of UO_2 fuel particles can be described as [25]

$$E = 2.26 \times 10^{11}[1 - 1.131 \times 10^{-4}(T - 273.15)][1 - 2.62(1 - D)] \tag{5}$$

where E is the elastic modulus, whose unit is Pa. T is the temperature in Kelvin and D is the theory density (92–98%). v is Poisson ratio which is set as 0.316.

The Misses hardening rule of UO_2 fuel particles is as the following [23]

$$\bar{\sigma} = \begin{cases} 66.9 - 0.0397T + (520.0 - 0.0386T)\bar{\varepsilon}_p & T \leqslant 1200\ ^\circ\mathrm{C} \\ 36.6 - 0.0144T + (139.5 - 0.0688T)\bar{\varepsilon}_p & T > 1200\ ^\circ\mathrm{C} \end{cases} \tag{6}$$

where $\bar{\sigma}$ is the Misses equivalent stress, whose unit is kg/mm^2; $\bar{\varepsilon}_p$ is the equivalent plastic strain.

The total swelling of fuel particles include three parts: gas-bubble swelling, solid fission product swelling and densification due to variation of the porosity [24–26].

$$\left(\frac{\Delta V}{V}\right)^{gs} = 439.6 \exp\left(-\frac{16,450}{T - 100}\right) \tag{7}$$

$$\left(\frac{\Delta V}{V}\right)^{ss} = 0.0025 \tag{8}$$

The above two expressions depict the volume fraction of gas-bubble swelling and solid fission product swelling per 10^{20} fissions/cm^3, and T is the temperature in kelvin.

$$\left(\frac{\Delta V}{V}\right)^{ds} = \{0.0142[1-\exp(-6.7943\mathrm{BU})] + 0.00893[1 - \exp(-1.1434\mathrm{BU})]\} \cdot \mathrm{ADST} \quad (9)$$

Expression (9) depicts densification of UO_2, where BU: burnup (MWD/kgUO_2), ADST: adjusting factor (=0.6).

2.3. The material model of the matrix and cladding

The matrix and cladding adopt the same material Zircaloy. The thermal expansion coefficient [21] is 5.58×10^{-6}/K. The Young's modulus and Poisson's ratio adopt Fisher Model [27]:

$$E = 9.9 \times 10^5 - 566.9 \times (T - 273.15) \times 9.8067 \times 10^4 \quad (10)$$

$$v = 0.3303 + 8.376 \times 10^{-5}(T - 273.15) \quad (11)$$

where E is Young's modulus (Pa), T is the temperature in Kelvin and v is Poisson's ratio.

The strain-hardening curve is described as [28]:

$$\sigma = K\varepsilon^n \cdot \left(\frac{\dot{\varepsilon}}{10^{-3}}\right)^m \quad (12)$$

where σ is the true stress, ε is the true strain, n is the strain-hardening exponent, K is strength coefficient and m is strain rate sensitivity exponent. $\dot{\varepsilon}$ is the true strain rate. If $\dot{\varepsilon} < 10^{-5}$/s, set $\dot{\varepsilon} = 10^{-5}$/s.

$$K = 1.0884 \times 10^9 - 1.0571 \times 10^6 T \quad (13)$$

$$n = -1.86 \times 10^{-2} + T(7.11 \times 10^{-4} - 7.721 \times 10^{-7} T) \quad (14)$$

$$m = 0.02 \quad (15)$$

where T is the temperature in Kelvin with the application range from 300 K to 730 K.

3. The finite element model

3.1. Selection of the Representative Volume Element and the finite element model

Similar to the modeling method of our previous work [21], the Representative Volume Element (RVE) as Fig. 1 can be selected with assuming that the fuel particles are periodically distributed along the length and width directions. For example, based on the assumption that the spherical particles are cubically arranged in the matrix illustrated as Fig. 2a, the Representative Volume Element (RVE) is selected as Fig. 2b according to the periodicity and the actual geometry shape that the sizes along the length and width directions are much larger than the one along the thickness direction. For the sake of calculation efficiency, the finite element model is developed according to the symmetry of the RVE to be 1/8 fraction of the RVE, shown as Fig. 2c. The plane $Z = 0$ expresses the mid-plane of the fuel plate and the plane with $Z = H/2$ denotes the upside surface which is the contact surface with the coolant water.

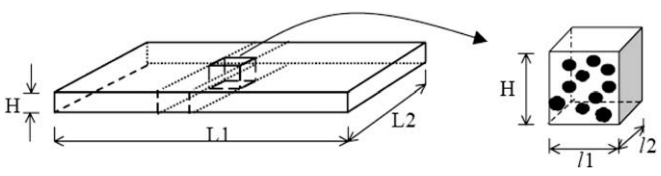

Fig. 1. Dispersion fuel plate and the Representative Volume Element.

In this study, the meat thickness is set as 1.27 mm and the cladding thickness maintains 0.4 mm. With the particle volume fraction in the fuel meat being 20% and with the particle distribution form being simple cubic, the finite element models are developed respectively for different particle diameters (50 μm, 100 μm and 200 μm), shown in Fig. 3. The fuel particles and the metal matrix are supposed to be bonded perfectly, and the bonding between the cladding and the fuel meat are also assumed to be perfect.

3.2. Mesh grid for the respective finite element models developed

The thermal–mechanical coupling element C3D8RT in the commercial software ABAQUS is used to discrete the finite element models. The mesh grids, the node and element information of the developed finite element models are presented in Fig. 3 and Table 1. Convergence of the computing results is investigated through checking the trend of the calculated results as a function of mesh size. The final discrete meshes are determined according to the convergence investigation in the meshes, therefore the obtained results in this study have been testified to have enough precision.

3.3. Boundary conditions

Since the mechanical analysis is directly coupled with the thermal analysis in this work, two sets of boundary conditions should be taken into account at the same time. The boundary conditions to determine the temperature field are given as

(1) Except the upside surface $Z = H/2$, the other surfaces of the finite element models all satisfy: $-k\frac{\partial T}{\partial n} = 0$.
(2) The upside surface $Z = H/2$ satisfy the convection boundary condition: $-k\frac{\partial T}{\partial n} = h(T - T_f)$, where the temperature of the coolant water T_f is 573 K and the heat transfer coefficient used is 2×10^{-2} W/mm^2 K.

The used boundary condition to determine the stress field is as the following:

(1) The symmetric boundary condition is applied at all the surfaces of the finite element models, except the upside surface $Z = H/2$.
(2) The continuous displacement conditions are met at the interfaces between the fuel particles and the matrix and the ones between the meat and the cladding.

3.4. Simulation method of the in-pile behaviors

At the initial stage of burnup, the mechanical behavior is mainly induced by the temperature difference between the steady state one and the room one. With increasing burnup, the irradiation swelling is the main factor to result in variation of the mechanical behaviors. Thus, the total burnup can be divided into two stages: the initial stage of burnup and the increasing stage of burnup. Thus, the total calculation is divided into two analysis steps.

The first analysis step is to model the mechanical behaviors at the initial stage of burnup. Firstly, the steady temperature field is solved, and then the displacement field, the strain field and the thermal stress field resulting from the temperature differences are calculated with the thermal-elastoplasticity method. In ABAQUS, the thermal–mechanical coupling element C3D8RT is chosen, the thermal and thermal–mechanical behaviors can be solved directly.

For the second analysis step, the irradiation-swelling simulation with increasing burnup becomes a key problem. The complexity exists in that: (1) the particle swelling will lead to appearance of

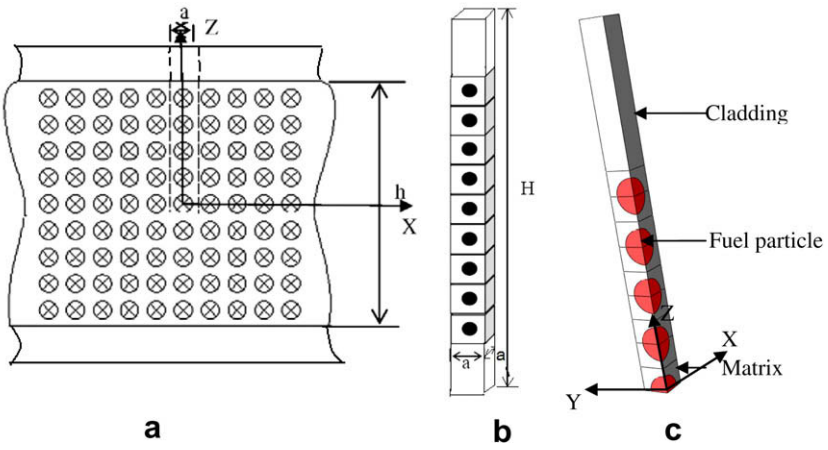

Fig. 2. (a) Sketch map, (b) RVE and (c) finite element model of the dispersion fuel plate.

Table 1 Element information for finite element models with different particle diameters

Particle diameter (um)	Element pattern	Number of elements	Number of nodes
50	C3D8RT	27007	31752
100	C3D8RT	23448	27727
200	C3D8RT	18408	21592

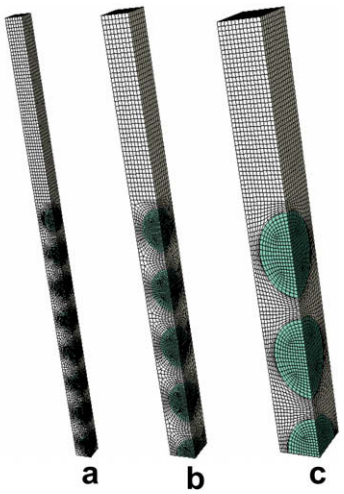

Fig. 3. Finite element models for different particle diameters (a) 50 um, (b) 100 um (c) and 200 um.

Table 1
Element information for finite element models with different particle diameters.

Particle diameter (um)	Element pattern	Number of elements	Number of nodes
50	C3D8RT	27,007	31,752
100	C3D8RT	23,448	27,727
200	C3D8RT	18,408	21,592

large strains in the metal matrix and variation of the fuel plate configuration; (2) the changed configuration will bring the temperature variations within the fuel plate. Due to this, the large-deformation finite element method is adopted and the Updated Lagrange Method is used. As a result, the second analysis step is divided into several time steps and the configurations of the finite element models are updated after every time step. At every time step, the steady-state temperature field is calculated once again; and the structural field is computed subsequently with considering variation of the temperatures with respect to the ones at the previous time step.

In ABAQUS, introduction of the irradiation swelling can be implemented by inputting a constant volumetric swelling strain rate of fuel particles. In the large-deformation finite element analysis, the volumetric swelling strain rate at every time step is corresponding to the updated configuration. As a result, the simulation method is proposed as follows.

The irradiation swelling of fuel particles at a certain burnup is defined as the relative volumetric change:

$$\mathrm{SW(BU)} = \frac{\Delta V}{V_0} \tag{16}$$

where BU denotes burnup (% FIMA), which depicts the ratio of the fissioned atoms to the total fissionable atoms, ΔV is the absolute volumetric change, V_0 is the initial volume.

Firstly, the irradiation swelling at a certain burnup SW(BU) is calculated out according to Eqs. (7)–(9), then the relation between the irradiation swelling and the virtual volumetric swelling strain rate is developed as the following.

The total calculation process is divided into $\boldsymbol{n}$ virtual time steps, ensuring that the strain increment and deformation at every step are small. At an arbitrary time step from time $\boldsymbol{t-1}$ to time $\boldsymbol{t}$, the ratio of the volume at time $\boldsymbol{t}$ to the volume at time $\boldsymbol{t-1}$ is set to be constant. That is,

$$\frac{V_t}{V_{t-1}} = \frac{V_{t-1} + \Delta V_t}{V_{t-1}} = 1 + \theta \tag{17}$$

where θ denotes the average volumetric strain induced by the irradiation swelling at every virtual time step. Then

$$\frac{V_n}{V_0} = \frac{V_1}{V_0}\cdot\frac{V_2}{V_1}\cdots\frac{V_n}{V_{n-1}} = (1+\theta)^n \tag{18}$$

$$\mathrm{SW(BU)} = \frac{V_n - V_0}{V_0} = (1+\theta)^n - 1 \tag{19}$$

Eq. (19) describes the relationship between the average volumetric strains of every virtual time step and the irradiation swelling at a certain burnup. In order to keep the small strain increment, the total number of the virtual time steps $\boldsymbol{n}$ should be set large enough. In the practical calculation, $\boldsymbol{n}$ is set to be a limit value at which θ tends to be a stable value. Consequently, the average volumetric swelling rate could be obtained

$$\dot{\theta} = \theta/1 \tag{20}$$

where 1 denotes a virtual time step size .

As a whole, the total computation of the in-pile behaviors is divided into two analysis step: (1) the first analysis step considers only the thermal effects; this analysis step is further divided into several time steps to calculate the thermal-elastoplastic behavior precisely; (2) the second loading step allows for the contribution of the irradiation swelling. And the volumetric swelling strain rate obtained according to Eqs. (16)–(20) is introduced into ABAQUS and enough time steps are divided.

4. Results and discussions

4.1. Validation of the simulation method

The numerical simulation results of the actual volumetric expansions at different burnups are compared with the theoretical ones of the irradiation swelling, as denoted in Fig. 4. It can be discovered that the actual volumetric expansion values are slightly higher than the theoretical computation results of the irradiation swelling; and after eliminating the thermal expansion effect, the obtained volumetric expansion values are very close to and briefly lower than the theoretical ones. This simulation result is reasonable in respect that: (1) the total deformation consists of four parts: the elastic one, the plastic one, the thermal expansion and the irradiation swelling, in which only the elastic deformation, the thermal expansion and the irradiation swelling contribute to the volumetric variations of fuel particles; (2) the elastic compressive deformation is very small, thus the main contributors of the volumetric variation are the thermal expansion and the irradiation swelling. Therefore, the actual volumetric expansions are higher than the theoretical values of irradiation swelling; (3) the volumetric expansion results without contribution of thermal expansions

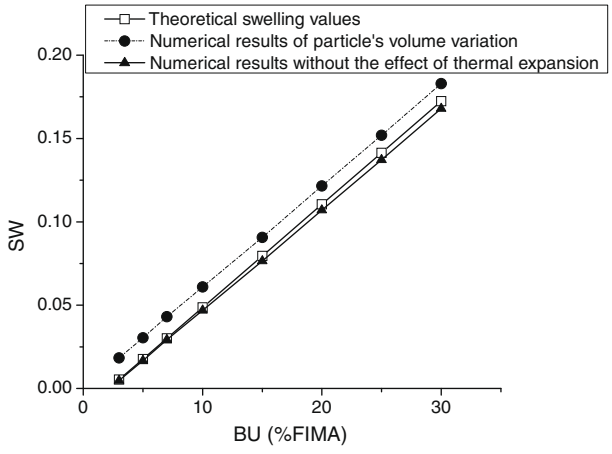

Fig. 4. The comparison of the theoretical results with the numerical simulation ones of the irradiation swelling.

are lower than the theoretical ones of irradiation swelling; and the differences seem to increase with the burnup; this is for the reason that the fuel particles are restrained by the metal matrix around to result in the elastic compressive strains within the fuel particles, and with increasing burnup the higher the irradiation swelling is, the larger the compressive strains are.

Based on the above analysis, it can be acquired that the irradiation-swelling simulation with ABAQUS is validated.

4.2. The in-pile mechanical behaviors with increasing burnup

4.2.1. Effects of particle diameters on the plate thickness variations

A key problem to affect the security of dispersion nuclear fuel plates is the plate thickness variations with increasing burnup. In order to avoid the loss-of-coolant accident, the increments of the plate thickness should be predicted. The plate thickness variations at different burnups for the considered particle diameter cases are shown as Fig. 5. The value at zero burnup takes the one induced by the thermal effect at the initial stage of burnup.

It can be found from Fig. 5a that: (1) for every considered case, the linear relation between the plate thickness increment and the burnup appears at the higher burnups; (2) at a certain burnup, the increment of the plate thickness increase with the particle diameter; and for the case with larger particle diameter, the increase rate is higher, which can be seen from the slope of the curves; (3) at 30% FIMA, the plate thickness increments reach 36.8 μm, 60.1 μm and 74.4 μm respectively for the three cases with d = 50 μm, d = 100 μm and d = 200 μm, they are 2.7 times, 3.4 times and 3.8 times as large as the plate thickness variations due to only the thermal effects. It can be found from Fig. 5b that with increasing particle diameters the plate thicknesses increase with the particle diameters at each burnup and this effect is strengthened at higher burnups from the view point of the slops of the curves.

It can be obtained that it is beneficial for reducing the plate thickness increment to use small-diameter particles within the fuel meat.

4.2.2. Effects of particle diameters on the plate temperatures

The maximum temperature within the fuel plate is at the midplane. The calculated maximum temperatures for different particle diameters are depicted in Fig. 6. The temperature at zero burnup in Fig. 6a gets from the first analysis step, that is, it is the result of the steady-state temperature at the initial stage of burnup. With increasing burnup, the plate configuration will change (as shown in Fig. 5) which can lead to the temperature variations. The temperature variations illustrated in Fig. 6 result from the configuration changes of the fuel plate. It can be found out from Fig. 6a that the maximum temperatures increase linearly with the burnup for each case; and compared to the temperatures at the initial stage of burnup, at 30% FIMA the maximum values increase only 5 K, 7 K and 10 K for the three cases with d = 50 μm, d = 100 μm and d = 200 μm. It can be also discovered that the increase rate with burnup for the maximum diameter case is the highest for the three considered cases. It can be discovered from Fig. 6b that the effect of particle diameters on the temperatures weakens with increasing the particle diameters, as can be obtained from the slopes of the curves.

To sum up, the larger the particle diameter is, the higher the internal temperatures exist at the fuel element and the higher the increase rate is.

4.2.3. Effects of particle diameters on the in-pile mechanical behaviors of the metal matrix

The contour plots of the equivalent plastic strains, the Mises stresses and the first principal stresses at 3% FIMA for d = 100 μm are shown in Fig. 7.

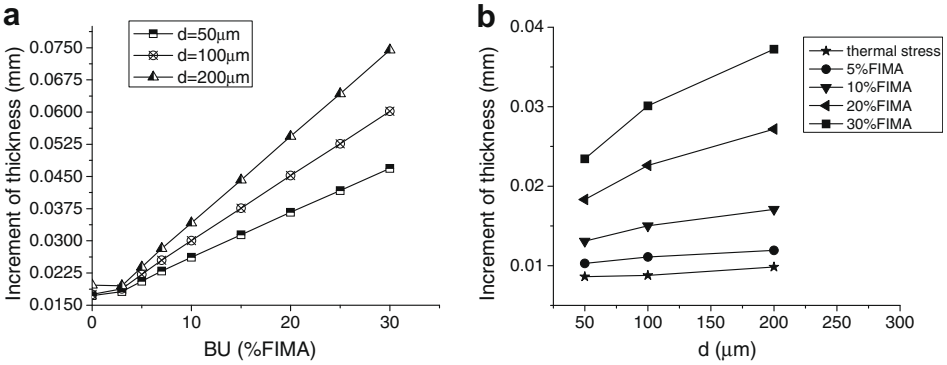

Fig. 5. (a) The plate thickness increments with increasing burnup for different particle diameters and (b) the ones with increasing the particle diameters at different burnups.

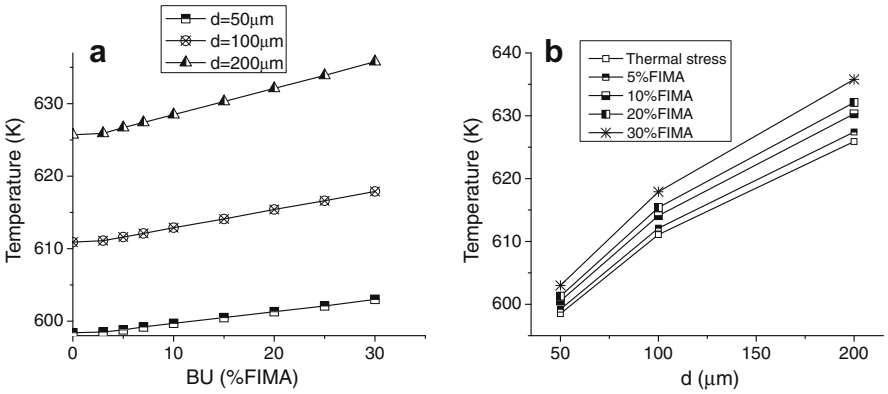

Fig. 6. (a) The variations of the maximum temperatures with increasing burnup for different particle diameters (b) the ones with increasing the particle diameters.

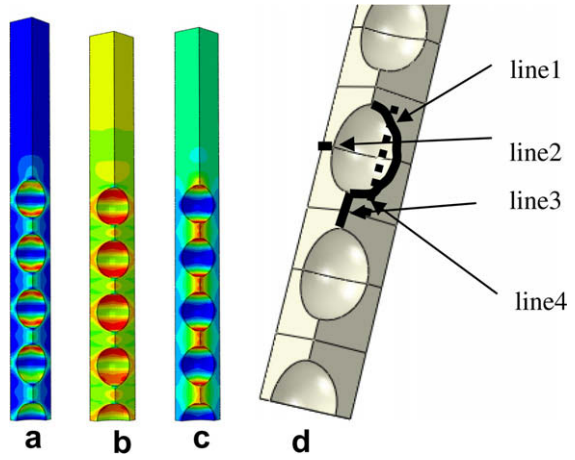

Fig. 7. The distributions of: (a) the equivalent plastic strains (b) the Mises stresses, (c) the first principal stresses at 3% FIMA and (d) the export paths of the results.

From Fig. 7, it can be found that for the Mises stresses and the equivalent plastic strains at 3% FIMA there are three larger regions at the metal matrix: (1) the interfaces between the metal matrix and the fuel particles; (2) the locations between the two particles along the length or width direction; (3) the positions between the two fuel particles along the thickness direction. With increasing burnup, the third region is in a state of plastic unloading, while the other two regions remain in a plastic loading state. Thus, line 1 and line 2 in Fig. 7d are chosen as the export paths of the Mises stresses and the equivalent plastic strains.

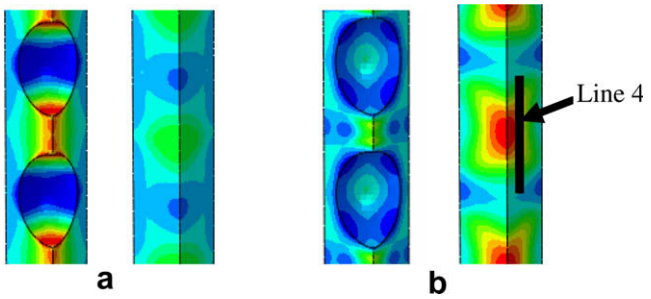

Fig. 8. The location variations of the maximum first principal stresses (a) at lower burnups and (b) at higher burnups.

It can be seen from Fig. 7c that the maximum tensile stresses at 3% FIMA exist in the locations between the two particles along the thickness direction. In fact, the above regions have the maximum tensile stresses at lower burnups, as is also shown in Fig. 8a; however, at higher burnups the maximum tensile stresses turn to the backside, because the first principal stresses at the original maximum regions decrease at higher burnups, as can be found in Fig. 8b. So, the locations of the maximum first principal stresses vary with the burnup. Thus, the maximum first principal stresses at the matrix are investigated without exporting the results along a specific path. The maximum first principal stresses are investigated for the metal matrix because the matrix materials are attacked continually by the fast neutron flux with increasing burnup and they might harden and embrittle. If the brittle fracture acts as its damage mode, the two regions mentioned above with the maximum tensile stresses are comparably dangerous.

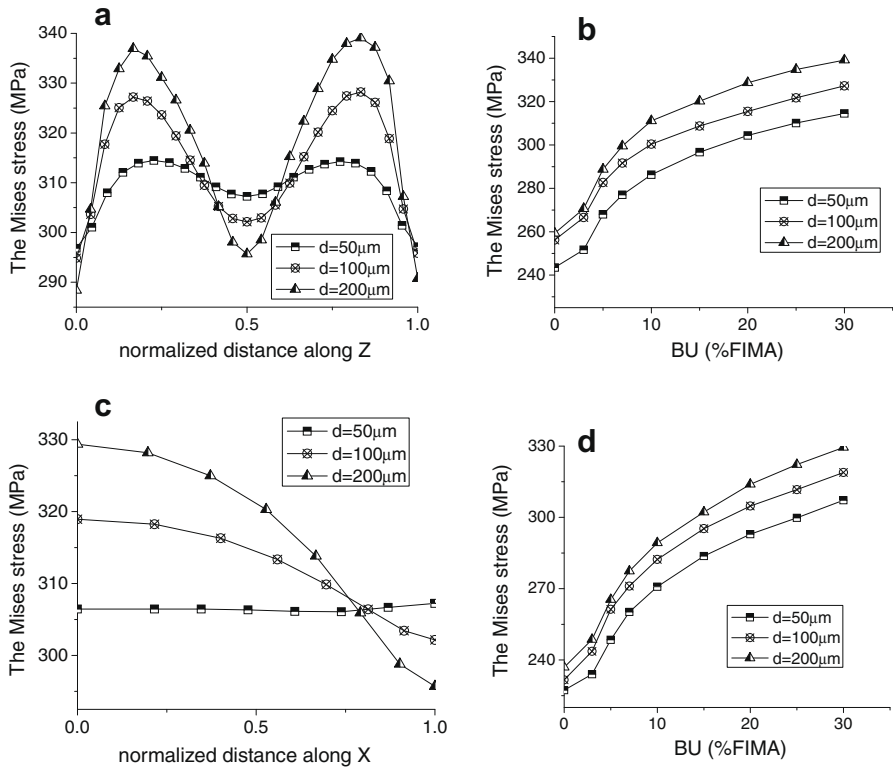

Fig. 9. Effects of particle diameters on the Mises stresses at the metal matrix (a) the Mises stress distribution along line 1 at 30% FIMA, (b) the maximum Mises stresses along line 1 at different burnups, (c) the Mises stress distribution along line 2 at 30% FIMA and (d) the maximum Mises stresses along line 2 at different burnups.

Based on the above analysis, in the following the Mises stresses and the equivalent plastic strains at line 1 and line 2 at different burnups will be given.

Fig. 9 illustrates the variations of the Mises stresses at different burnups for the three considered cases. Fig. 9a and c show the Mises stress distributions along line 1 and line 2 at different burnups, respectively, in which the transverse coordinates use the normalized ones. The normalized transverse coordinates of Fig. 9a are defined as $z_{normalized} = \frac{z-z_{low}}{z_{high}-z_{low}}$, in which z_{high}, z_{low} express the z coordinates of the upside point and the downside one at line 1. And the normalized transverse coordinates of Fig. 9c is defined as $x_{normalized} = \frac{x-x_{left}}{x_{right}-x_{left}}$, in which x_{right}, x_{left} denote the x coordinates of the right point and the left point at line 2. And the variations of the maximum Mises stresses along line 1 and line 2 with increasing burnup are illustrated as Fig. 9b and d.

It can be found from Fig. 9a and c that the maximum Mises stresses at the two paths increase with the particle diameters; the maximum values at line 1 are always larger than the ones at line 2; at line 1, for every considered case the locations with the maximum Mises stresses keep near the separate point between the metal matrix and the fuel particles along the thickness direction; for line 2, different distributions exist: (1) at 30% FIMA, the maximum value for the case $d = 50$ μm locates at the interface; (2) while the maximum values for the other two cases appear in the middle of the joint line of the centers of the two fuel particles along the length or width direction; (3) it should be pointed out that the maximum value locations for the case $d = 50$ μm are varied with increasing burnup, its maximum value locations at lower burnups are the same to the other two cases and they are shifted toward the interface with an increase of burnup. From the view point of increments of the stress value, at 30% FIMA the maximum value for the case with $d = 100$ μm is 12 MPa more than the one for $d = 50$ μm, and the maximum value for $d = 200$ μm is 11 MPa more than the one for $d = 100$ μm; the increase trend with the particle diameter gets weaker, as can be clearly found from the slopes of the curves in Fig. 10.

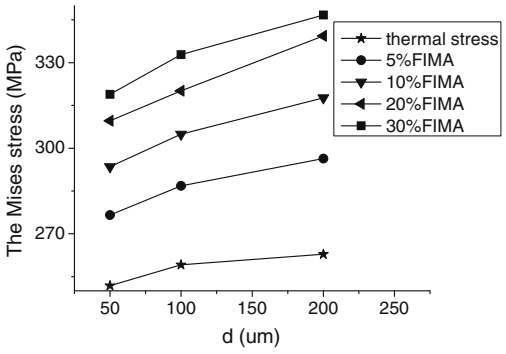

Fig. 10. The Mises stress variations with increasing the particle diameters.

The variations of the maximum Mises stresses for each case with increasing burnup are depicted in Fig. 9b and d. For each case, it can be obtained that the maximum values increase with the burnup and the increasing slops maintain steady between 10% FIMA and 30% FIMA, as can be seen from Fig. 9b; and at a certain burnup, the larger the particle diameter is, the higher the Mises stresses attain.

The effects of particle diameters on the equivalent plastic strains are denoted as Fig. 11. It can be found from Fig. 11a that the strain values for the case $d = 100$um and the case $d = 200$ μm are much larger the ones for the case $d = 50$ μm. As is shown in Fig. 11a, the maximum equivalent plastic strain for the case $d = 100$ μm is 1.6 times as large as the one for the case $d = 50$ μm; and the one for the case $d = 200$ μm is 3.3 times, in-

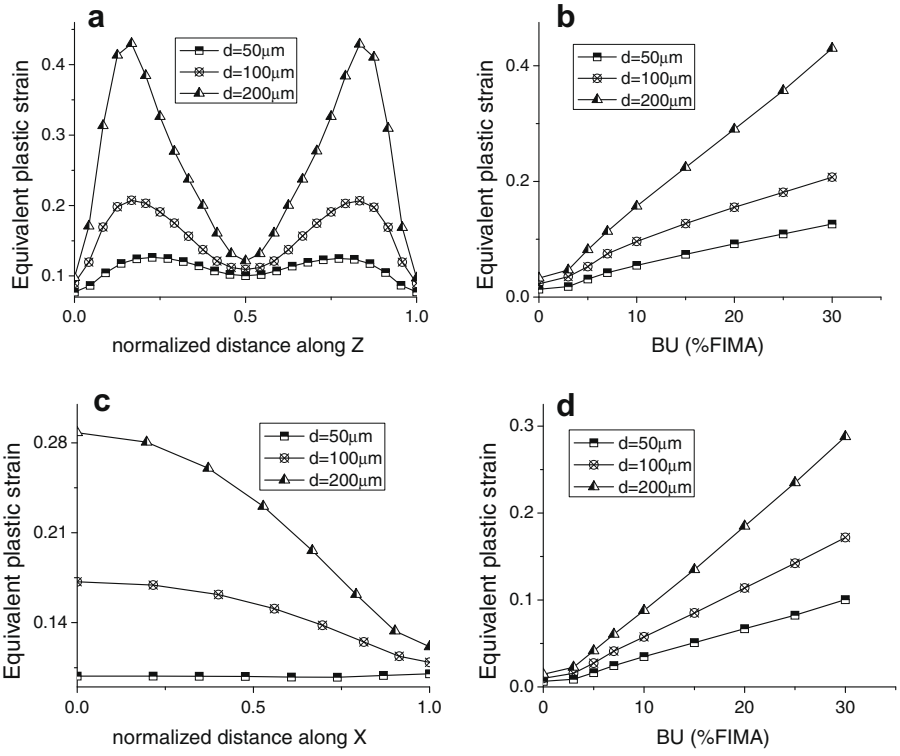

Fig. 11. Effects of particle diameters on the equivalent plastic strains at the matrix (a) the equivalent plastic strains along line 1 at 30% FIMA, (b) the maximum equivalent plastic strain variations along line 1 with increasing burnup, (c) the equivalent plastic strains along line 2 at 30% FIMA and (d) the maximum equivalent plastic strain variations along line 1 with increasing burnup.

stead; the maximum equivalent plastic strain for the case $d = 200$ μm reach 43%. Similar to the Mises stress distribution, it can be observed from Fig. 11c that at 30% FIMA the maximum equivalent plastic strains at line 2 for the two cases with $d = 100$ μm and $d = 200$ μm appear in the middle of the center joint lines of the two fuel particles along the length or width direction, while for the case with $d = 50$ μm, the maximum strain value locate near the interface. For the two cases with $d = 100$ μm and $d = 200$ μm, their maximum equivalent plastic strains are 1.5 times and 2.8 times of the one for the case $d = 50$ μm, as is illustrated in Fig. 11c.

It can be discovered from Fig. 11b and d that at higher burnups the equivalent plastic strains take on a linear relation with the burnup; and the equivalent plastic strain values increase distinctly with increasing burnup; compared to the equivalent plastic strains at 3% FIMA, the maximum values at line 1 for the three cases ($d = 50$ μm, 100 μm, 200 μm) at 30% FIMA are 9 times, 9 times and 13 times of the former (at 3% FIMA), and the maximum strain values at line 2 are 16.6 times, 17.7 times and 19.7 times of their relative values at 3% FIMA; it can be deduced that the maximum equivalent plastic strains at line 2 increase quicker than the ones at line 1. The variations of the maximum equivalent plastic strains at the matrix with increasing the particle diameters are denoted as Fig. 12. It can be discovered that the increase rates of the maximum equivalent plastic strains rise with the particle diameters.

The variations of the first principal stresses with the particle diameters are of complexity. With increasing burnup, the locations of the maximum values of the first principal stresses for the considered three cases do not agree with each other. Here the locations of their maximum values are not investigated. The variations of the maximum values with the burnup are given as Fig. 13. It can be found that the maximum first principal stresses for each case ($d = 50$ μm, $d = 100$ μm and $d = 200$ μm) increase with the burnup and the increase rates turn slower, as can be seen from

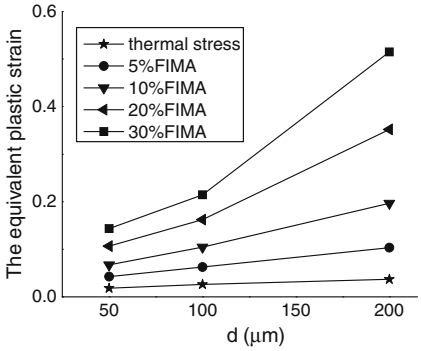

Fig. 12. Variations of the maximum equivalent plastic strains at the matrix.

the slops of the curves. At the initial stage of burnup, the larger the particle diameter is, the larger the first principal stresses exist; while at the increasing stage of burnup, the increase rates for the case with $d = 50$ μm are quicker than the ones for the case with $d = 100$ μm and the first principal stresses of the former are larger than the ones of the latter at the burnups higher than 8% FIMA; the first principal stresses for the case with $d = 200$ μm are always much larger than the other two cases, its value reach 600 MPa at 30% FIMA which is much higher than the ones of the two cases with 315 MPa for $d = 50$ μm and 285 MPa for $d = 100$ μm.

4.2.4. Effects of particle diameters on the in-pile mechanical behaviors of the cladding

The export path at the cladding is chosen, as is depicted in Fig. 14, which is from the separate point of the fuel meat and the cladding to the outside surface. Owing to the scarce variations with increasing the burnup at the points a bit far from the interface

point, a part of the export path is regarded as the actual export of the results. The Mises stresses, the equivalent plastic strains and the first principal stresses with increasing the burnup for the three cases with $d = 50$ μm, $d = 100$ μm and $d = 200$ μm are depicted as Fig. 15–17.

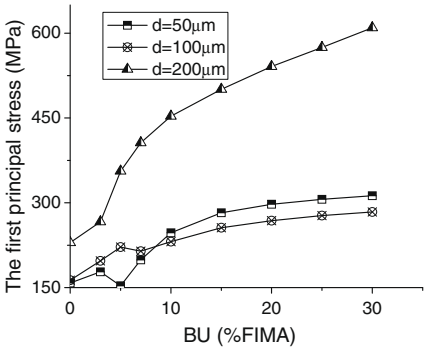

Fig. 13. Effects of particle diameters on the first principal stresses at the matrix.

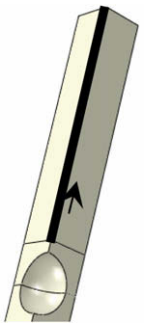

Fig. 14. The export path at the cladding.

The Mises stress variations are shown as Fig. 15. It can be observed from Fig. 15a that for the case with $d = 50$ μm, the maximum value exists at the interface points with the fuel meat and the Mises stresses decrease along the export path at the initial stage of burnup; however, with increasing the burnup the Mises stresses close to the interface point decrease to be the minimum value at the export path; at the burnups higher than 20% FIMA, the relative stress values near the interface point increase instead. For the case with $d = 100$ μm, it can be found from Fig. 15b that the maximum Mises stress induced only by the thermal effects locates at the interface point; at the burnups between 5% FIMA and 10% FIMA, the Mises stresses decrease, but the maximum values are still in the vicinity of the interface point; at the burnups higher than 10% FIMA, the Mises stresses nearby the interface points continually decrease and the maximum values locate at the large part of the region near the outer surface. It can be clearly seen from Fig. 15c that the Mises stress variations for the case with $d = 200$ μm are different from the other two cases: (1) the maximum Mises stresses occur near the interface point and the relative values increase with the burnup; and (2) the Mises stresses rapidly attenuate along the export path.

The effects of particle diameters on the maximum Mise stresses for the considered three cases are denoted as Fig. 15d. It can be found out that the maximum values for the two cases with $d = 50$ μm and $d = 100$ μm decrease with the burnup; while the maximum values for the case with $d = 200$ μm increase with the burnup and the increase rates become quicker; at the burnups lower than 10% FIMA, the larger the particle diameter is, the larger the maximum Mises stresses exist; at the burnups higher than 10% FIMA, the maximum Mises stresses for the case with $d = 100$ μm are the minimum and locate at the outer surface.

The effects of particle diameters on the equivalent plastic strains are given as Fig. 16. It can be discovered form Fig. 16a

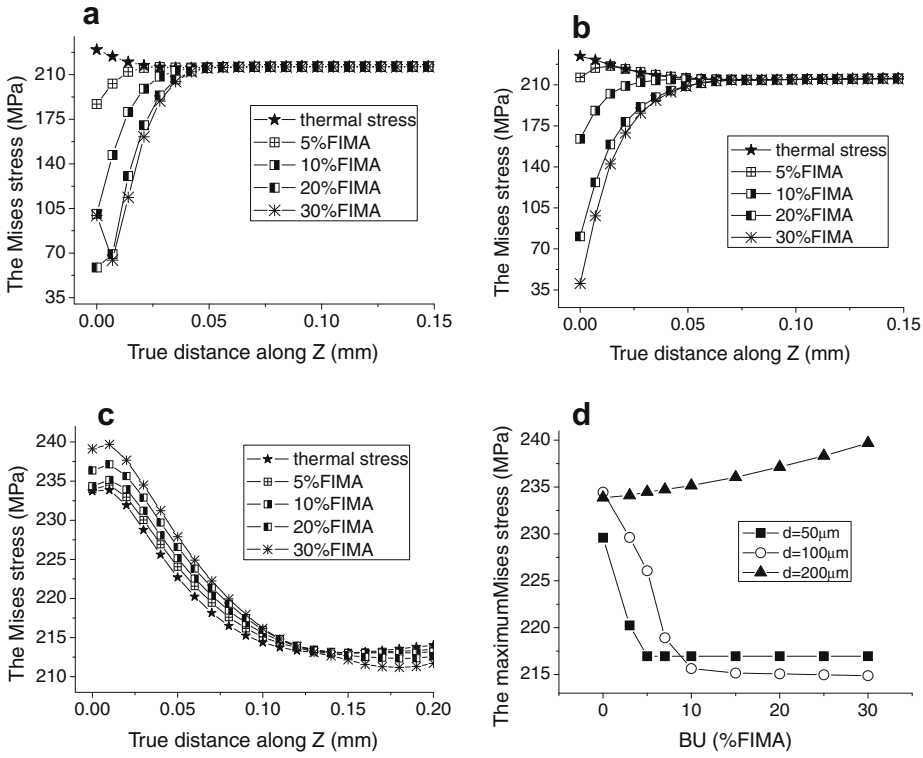

Fig. 15. Effects of particle diameters on the Mises stresses at the cladding (a) the results along the export path for $d = 50$ μm, (b) the results along the export path for $d = 100$ μm, (c) the results along the export path for $d = 200$ μm and (d) the variations of the Mises stresses with the particle diameters and burnups.

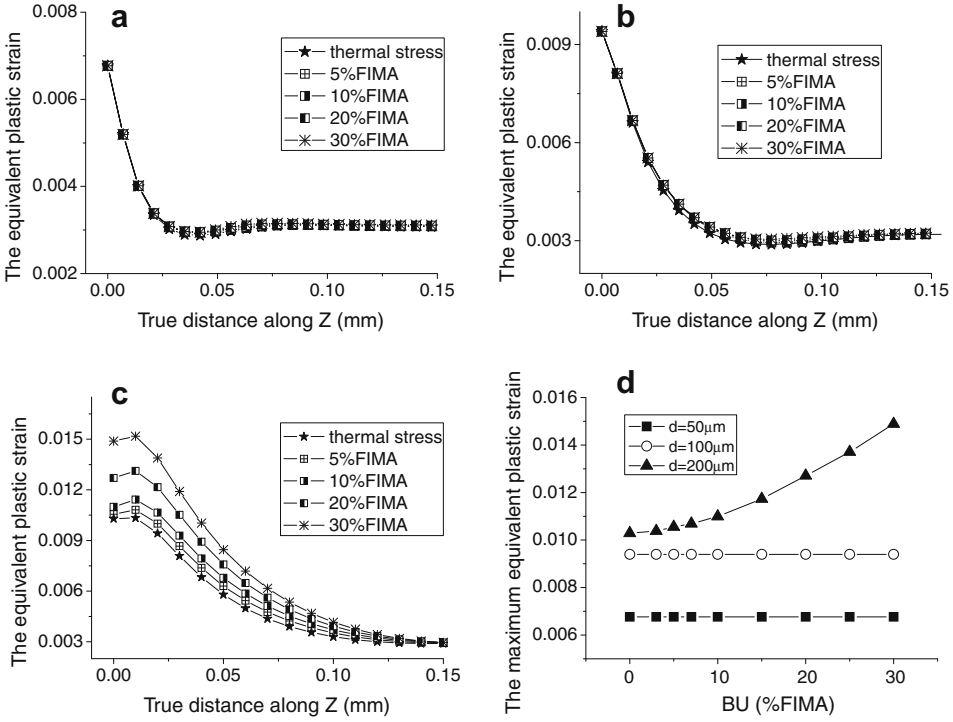

Fig. 16. Effects of particle diameters on the equivalent plastic strains at the cladding (a) the results along the export path for $d = 50$ μm, (b) the results along the export path for $d = 100$ μm, (c) the results along the export path for $d = 200$ μm and (d) the variations of the maximum equivalent plastic strains with the particle diameters and burnups.

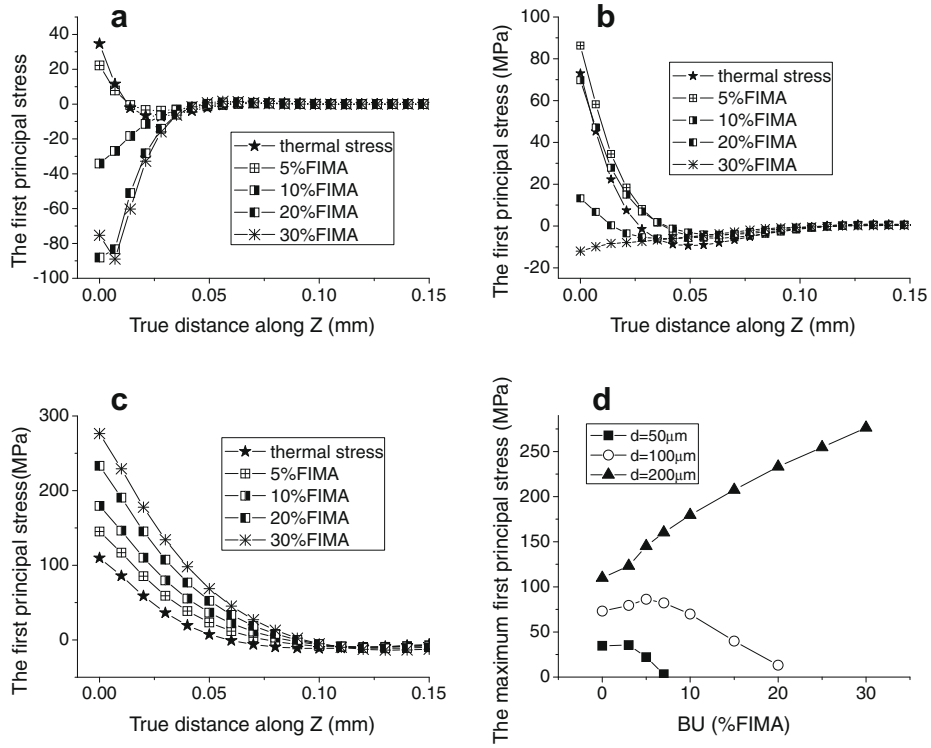

Fig. 17. Effects of particle diameters on the first principal stresses at the cladding (a) the results along the export path for $d = 50$ μm, (b) the results along the export path for $d = 100$ μm, (c) the results along the export path for $d = 200$ μm and (d) the variations of the maximum tensile stresses with the particle diameters and burnups.

and c that the distribution cures with increasing burnup almost superpose each other for the cases with $d = 50$ μm and $d = 100$ μm, and the equivalent plastic strains near the interface points have no changes, it can be obtained that the region near the interface with the fuel meat keeps at a plastic loading state with the Mises stresses decreasing with the burnup from the values induced by the thermal effects. As far as the case with $d = 200$ μm is concerned, it can be found from Fig. 16c that its max-

imum values locate near the interface point and the equivalent plastic strains increase with the burnup; the maximum value increase 40% more than the one due to the thermal effects. It can be observed from Fig. 16d that the maximum equivalent plastic strains increase with the particle diameters and the increase rates for the case with $d = 200$ μm turn to be higher and higher with increasing burnup.

The effects of the particle diameters on the first principal stresses at the cladding are shown in Fig. 17. For the case with $d = 50$ μm, it can be found that the maximum first principal stresses (tensile stresses) exist at the interface between the cladding and the fuel meat at the initial stage of burnup, and decrease toward zero along the export path direction; with increasing burnup, the first principal stresses near the interface continually decrease to negative values; at the burnups higher than 10% FIMA, only the compressive stresses occur at the cladding and the fracture induced by the tensile stresses might not happen. For the case with $d = 100$ μm, it can be seen from Fig. 17b that at the burnups between 5% FIMA and 20% FIMA larger tensile stresses exist in the vicinity of the interface and decrease along the export path direction; at 30% FIMA these is no tensile stress at the cladding. Different from the other two cases, there exist much larger tensile stresses near the interface for the case with $d = 200$ μm and their values increase with the burnup; the maximum values achieve about 300 MPa at 30% FIMA. It can be observed from Fig. 17d that the maximum tensile stresses increase with the particle diameters and the variation trends have great differences. It means it might be of highest possibility for the largest particle diameter ($d = 200$ μm)case to undergo fracture between the cladding and the meat.

4.2.5. Effects of particle diameters on the mechanical behaviors at the fuel particles

The effects of the particle diameters on the in-pile mechanical behaviors at the fuel particles are also notable. As far as the first principal stresses are concerned, it can be obtained from the numerical results that: (1) for the cases with $d = 50$ μm and $d = 100$ μm, the maximum first principal stresses with about 100 MPa only exist at the initial stage of burnup; with increasing the burnup the first principal stresses at the fuel particles rapidly decrease to become the compressive stresses and the fuel particles stay at a compressive state in all directions; (2) for the case with $d = 200$ μm, the maximum first principal stresses increase with the burnup and their values achieve 335 MPa at 30% FIMA.

The effects of particle diameters on the maximum Mises stresses at the fuel particles are illustrated as Fig. 18. It can be found that: (1) for the cases with $d = 50$ μm and $d = 100$ μm, the maximum values appear at about 7% FIMA, afterwards they decrease with burnup until 25% FIMA, and after 25% FIMA the maximum Mises stresses have the trends to increase again; (2) for the case with $d = 200$ μm, the maximum Mises stresses monotonously increase with burnup; (3) at 30% FIMA, the maximum Mises stress for the case with $d = 50$ μm is 168 MPa less than the one induced by the thermal effect; the one for the case with $d = 100$ μm is only 5 MPa lower than the result induced by the thermal effect; the maximum Mises stress for the case with $d = 200$ μm reach 541 MPa, which is 88 MPa more than the one due to the thermal effect. And it can also be found that the maximum Mise stresses increase with the particle diameters.

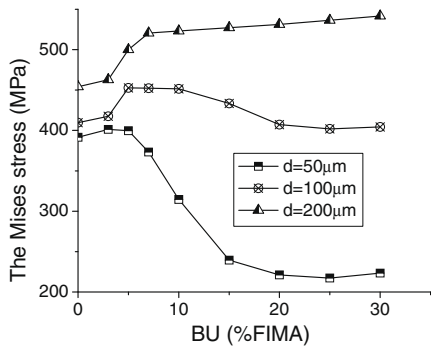

Fig. 18. Effects of particle diameters on the maximum Mises stresses at the fuel particles.

5. Conclusions

In order to evaluate the effects of fuel particle diameters on the in-pile mechanical behaviors of plate-type dispersion nuclear fuel elements with increasing burnup, a simulation method is developed for prediction of the in-pile mechanical behaviors. Allowing for the interactions between the fuel particles and the matrix and the one between the fuel meat and the cladding, the three-dimensional finite element models are constructed for different particle diameter cases; and the thermo–elasto-plasticity finite element method for large-deformation is adopted. Through numerical simulation, the main conclusions can be drawn as the following:

(1) The internal temperatures increase with the particle diameters.
(2) At the matrix, the maximum Mises stresses and equivalent plastic strains increase with the particle diameters; the effects of fuel particle diameters on the maximum first principal stresses vary with burnup, as a whole, the considered case with the largest particle diameter holds the maximum values all along.
(3) With increasing burnup, main variations of the Mises stresses and the first principal stresses take place at the cladding near the interface between the fuel meat and the cladding, and different variations exist for different particle diameter cases.
(4) The maximum Mises stresses within the fuel particles increase with the particle diameters, different particle diameter cases experience different variations with increasing burnup.

Acknowledgement

The authors appreciate the supports of the Natural Science Foundation of China (10772049, 10672042), Research and Development Program of China (863 Program, 2009AA04Z408), the Natural Science Foundation of Shanghai (06ZR14009), the Pujiang Scholar Program, and the Wangdao Scholar Program (08076) of Fudan University.

References

[1] Klaas Bakker, Frodo C. Klaassen, Ronald P.C. Schram, et al., Nuclear Technology 146 (2004) 325–331.
[2] A. Vatulin, V. Lysenko, V. Kostomarrov, V. Sirotin, Journal of Nuclear Materials 274 (1999) 135–138.
[3] Lee Van Duyn, Evaluation of the Mechanical Behavior of a Metal–matrix Dispersion Fuel for Plutonium Burning. A Thesis for the Degree Master of Science in Mechanical Engineering, Georgia Institute of Technology, 2003.
[4] V.P. Sinha, G.J. Prasad, P.V. Hegde, R. Keswani, C.B. Basak, S. Pal, G.P. Mishra, Journal of Alloys and Compounds 473 (2009) 238–244.
[5] F. Huet, V. Marelle, J. Noirot, P. Sacristan, P. Lemoine, in: Proceedings of the 2003 International Meeting on Reduced Enrichment for Research and Test Reactors, Chicago, IL, 5–10 October 2003.
[6] H.J. Ryu, Y.S. Han, J.M. Park, S.D. Park, C.K. Kim, Journal of Nuclear Materials 321 (2003) 210.
[7] A. Leenaers, S. Van den Berghe, E. Koonen, et al., Journal of Nuclear Materials 335 (2004) 39.

[8] F. Huet, J. Noirot, V. Marelle, S. Dubois, P. Boulcourt, P. Sacristan, S. Naury, P. Lemoine, in: Proceedings of the Ninth International Topical Meeting on Research Reactor Fuel Management, Budapest, Hungary, 10–13 April 2005.
[9] Chan Bock Lee, Yong Sik Yang, Dae Ho Kim, Sun Ki Kim, Je Geun Bang, Journal of Nuclear Science and Technology 45 (1) (2008) 60–71.
[10] S.J. Oh, K.H. Kim, S.J. Jang, D.B. Lee, Y.S. Lee, J.M. Park, H.D. Park, C.K. Kim, The development of U-7 wt.% Mo for large particle powers by centrifugal atomization, RRFM2006 Transactions, Session 2, Poster Fuel Development, pp. 136–140.
[11] J.L. Snelgrove, G.L. Hofman, M.K. Meyer, C.L. Trybus, T.C. Wiencek, Nuclear Engineering and Design 178 (1997) 119–126.
[12] H. Taboada, J. Rest, M.V. Moscarda, M. Markiewicz, E. Estevez, in: Proceedings of the 24th International Management on Reduced Enrichment for Research and Test Reactors, San Carlos de Bariloche, Argentina, 3–8 November 2002.
[13] J. Rest, The DART Dispersion Analysis Research Tool: A Mechanistic Model for Predicting Fission-Product-Induced Swelling of Aluminum Dispersion Fuels, ANL-95/36, 1995.
[14] S.L. Hayes, M.K. Meyer, G.L. Hofman, J.L. Snelgrove, R.A. Brazener, in: Proceedings of the 2003 International Meeting on Reduced Enrichment for Research and Test Reactors, Chicago, IL, 5–10 October 2003.
[15] S.L. Hayes, G.L. Hofman, M.K. Meyer, J. Rest, J.L. Snelgrove, in: 2002 International Meeting on Reduced Enrichment for Research and Test Reactors, Bariloche, Argentina, 3–8 November 2002.
[16] V. Marelle, S. Dubois, M. Ripert, J. Noirot, P. Lemoine, in: The RERTR-2007 International Meeting on Reduced Enrichment for Research and Test Reactors, 23–27 September, Diplomat Hotel – Prague, Prague, Czech Republic, 2007.
[17] V. Marelle, F. Huet, P. Lemoine, in: Proceedings of the Eighth International Topical Meeting on Research Reactor Fuel Management, München, Germany, 21–24 March 2004.
[18] Roberto Saliba, Horacio Taboada, Ma. Virginia Moscarda, in: 2003 International Meeting on Reduced Enrichment for Research and Test Reactors, Chicago, IL, 5–10 October 2003.
[19] K. Böning, W. Petry, Journal of Nuclear Materials 383 (2009) 254–263.
[20] Shurong Ding, Xin Jiang, Yongzhong Huo, Lin Li, Journal of Nuclear Materials 374 (2008) 453–460.
[21] Shurong Ding, Yongzhong Huo, XiaoQing Yan, Journal of Nuclear Materials (2009), doi:10.1016/j.jnucmat.2009.04.015.
[22] P.G. Lucuta, H.S. Matzke, I.J. Hastings, Journal of Nuclear Materials 232 (1996) 166–180.
[23] MATPRO-09, A Handbook of Materials Properties for Use in the Analysis of Light Water Reactor Fuel Rod Behavior, USNRC TREE NUREG-1005, 1976.
[24] W. Chubb, V.W. Storhok, D.L. Keller, Nuclear Technology 18 (1973) 231–255.
[25] T. Nakajima, M. Ichikawa, et al., FEMAXI-III: A Computer Code for the Analysis of Thermal and Mechanical Behavior of Fuel Rods, AERI-1298, 1985.
[26] W. Wiesenack, M. Vankeerberghen, R. Thankappan, Assessment of UO_2 Conductivity Degradation Based on In-pile Temperature Data, HWR-469, 1996.
[27] E.F. Fisher, C.J. Renken, Physical Review 10 (1954) A482–A494.
[28] D.L. Hagrman, G.A. Reyman, MATPRO-Version11, A Handbook of Materials Properties for use in the Analysis of Light Water Reactor Fuel Rod Behavior, NUREG/CR-0497, TREE-1280, Rev.3, 1979A.